

# Machine Learning Approach to Predict tDCS-induced Electric Current in the Human Brain

Thesis

Submitted in partial fulfillment of the requirements for the Master's Degree  
in Data Science and Engineering

at

The City College of The City University of New York

by

Chikako Olsen

Approved by

Dr. A. Duke Shereen, Thesis Advisor

Professor Michael Grossberg

Professor Zhigang Zhu

Co-Directors, Data Science and Engineering Program

May 2023

# Machine Learning Approach to Predict tDCS-induced Electric Current in the Human Brain

Chikako Olsen

Data Science and Engineering Program

Thesis Advisor:

Dr. A. Duke Shereen

## Abstract

**Background:** Transcranial direct current stimulation (tDCS) is a promising non-invasive method for treating neurological and psychiatric disorders and enhancing cognitive function. However, the underlying mechanisms of tDCS are not fully understood, and there is no ground truth for determining, non-invasively, where in the brain tDCS electrical currents flow. At the same time, effective neuronal engagement from tDCS requires accurate localization of the induced currents to specific brain target regions. Machine Learning (ML) has the potential to significantly improve the accuracy and precision of tDCS current prediction. This study aims to develop a novel approach using ML to predict the location and strength of tDCS-induced currents in individual subjects.

**Methods:** A ring of current-carrying wire wrapped about the circumference of a cylinder containing fluid of high MRI signal is used to establish a theoretical ground truth for ML training, and a spherical phantom with electrodes at opposite ends of its equator is used to evaluate ML models. The cylindrical phantom provides ground truth for both the electric current and the magnetic field induced in the cylinder from the current since the magnetic field is well-known from the Biot-Savart Law, and the electric current is localized to the geometry of the circle of wire with a magnitude that is precisely measurable and controllable. The spherical phantom mimics an ideal scenario closer to the human brain as the current flows through the sphere (volume conduction) rather than being tightly constrained to the wire as in the cylinder case. Different regression models and deep learning techniques, including optimization, are utilized to develop optimal ML models using only data from the cylindrical phantom. ML performance in predicting the magnetic field induced by electric current in the cylinder, sphere, and human subjects is compared to traditional MRI measurements and computational modeling.

**Results:** The Multi-layer Perceptron (MLP) model emerged as the top-performing regression model in this study, achieving an impressive correlation score of 0.97 between prediction and ground truth on cylinder phantom data after optimization. The optimal MLP model consistently demonstrated strong correlations, reaching a maximum of 0.98, an average of 0.96, and a standard deviation of 0.026 for prediction and computer simulation within the regions of interest (ROI) of spherical phantom data. Additionally, the mean correlation between prediction and MRI measurement was 0.99, indicating they are close to identical. When applied to the human brain, the highest correlation between prediction and computer simulation reached 0.87 in the ROI, with an average correlation

of 0.59 and a standard deviation of 0.242. Furthermore, the correlation between our prediction and MRI measurement yielded a maximum value of 0.86, with an average correlation of 0.74 and a standard deviation of 0.166. These findings showcase the excellent performance of our prediction model on ROI from spherical phantom and human brain datasets.

**Conclusion:** The study demonstrates that a Multi-layer Perceptron Neural Network model trained solely on the cylindrical phantom dataset can effectively predict the tDCS-induced magnetic field in the human brain, reducing noise while preserving the characteristics of MRI measurement. However, the outcomes are influenced by the selection of the brain region of interest, indicating the need for further enhancements to create a comprehensive model that applies to the entire brain. Future work to calculate current density from the magnetic field using Maxwell's equations will benefit from these enhancements. Nonetheless, this research establishes that machine learning offers a proof of concept of a promising approach for predicting tDCS-induced currents.

**Keywords:** tDCS, MRI field mapping, machine learning

## **Acknowledgment**

This work was part of the project supported by the National Institutes of Health/ National Institute on Neurological Diseases and Stroke (1R21NS115018).

# Table of Contents

<b>Abstract</b>	1
<b>Acknowledgment</b>	4
<b>Table of Contents</b>	5
<b>List of Tables</b>	7
<b>Chapter 1: Introduction</b>	8
1.1 Overview	8
1.2 Problem Statement	9
<b>Chapter 2: Related Work</b>	10
<b>Chapter 3: Approach</b>	12
3.1 Subjects	12
3.2 Method	14
3.3 Design	16
<b>Chapter 4: Machine Learning Development with Cylinder Dataset</b>	17
4.1 Machine Learning Model Selection	17
4.2 Optimization	18
4.3 Evaluation	19
4.4 Quantitative Result for Machine Learning Testing	20
<b>Chapter 5: Machine Learning Evaluation on Spherical Phantom</b>	24
5.1 Sphere ROI Images Comparison	24
5.2 Analysis of Spherical Data Prediction	25
<b>Chapter 6: Prediction on Human Brain</b>	29
6.1 Human Brain ROI Image Comparison	29
6.2 Analysis of Human Brain Prediction	31
6.3 Analysis of Three Subjects	33
<b>Chapter 7: Discussion and Conclusion</b>	35
7.1 Discussion	35
7.2 Future Work	36
7.3 Conclusion	36
<b>Bibliography</b>	37
<b>Appendix</b>	42

## List of Figures

1 Phantom setup	13
2 R squared of predicted value against target value on each machine learning model	17
3 Heatmap of layer vs. unit based on Correlation, Standard Error, and Mean Squared Error on MLP	18
4 MLP model evaluation	20
5 The magnetic field images of the cylinder phantom ROI along Bx	21
6 The magnetic field images of the cylinder phantom ROI along Bx in reversed polarity	21
7 Correlation plots on the cylinder phantom ROI	23
8 The magnetic field images of the spherical phantom along Bz	25
9 The magnetic field images of the spherical phantom along Bz in reversed polarity	25
10 Correlation plots on the sphere phantom ROI	26
11 The magnetic field images of the human brain	30
12 The magnetic field images of the human head	31
13 Correlation plots on the human brain ROI	32
14 The magnetic field images of three human subjects	34

## List of Tables

1	Hyperparameters for Grid Search	19
2	Correlations comparison of the sphere ROI for three experiments	28
3	Correlations comparison of the sphere ROI and the whole sphere	29
4	Correlation comparison of the human brain ROI and the entire brain	33
5	Correlation comparison of the human brain ROI of three subjects	35
A1	Correlation comparison of the entire brain of three subjects	42

# **Chapter 1**

## **Introduction**

### **1.1 Overview**

Transcranial direct current stimulation (tDCS) is non-invasive brain stimulation that induces electrical current directly to a specific brain area(s). TDCS has been used not only to improve symptoms of neurological and psychiatric disorders, such as Alzheimer's disease [1] and depression [2] but also to enhance cognitive function, such as learning and working memory, in healthy subjects [3]. TDCS has recently become popular among researchers because of its low cost, safety, and usability. However, more research is needed to better understand the mechanisms of action of tDCS and improve its efficacy.

Machine learning has impacted various domains, including the medical industry. For example, pattern recognition and classification allow the diagnosis of brain tumors [4] and Alzheimer's disease [5] from magnetic resonance imaging (MRI) data. Moreover, machine learning can predict medical conditions such as diabetes [6] at an early stage. However, there is a paucity of published literature that employs machine learning to predict the electric and/or magnetic fields induced in the brain by non-invasive transcranial stimulation such as transcranial magnetic stimulation, and less work has been done specifically with application to tDCS [7][8][9]. Utilizing machine learning opens up the possibility of replacing the current state-of-art computational simulations and enabling accurate mapping of the electric/magnetic field in the individual human brain. The thesis aims to develop a machine learning approach to accurately predict the location and magnitude of the electric current generated by tDCS in individual subjects.

## 1.2 Problem Statement

Despite the growing interest and potential benefits of tDCS, several critical issues still need to be resolved. First, tDCS efficacy relies on delivering the appropriate current intensity to the target brain region. However, the precise electric current pathways within the human brain still need to be fully understood and accurately known. Secondly, accurately predicting the optimal tDCS current for an individual remains a challenge, requiring personalized approaches. For example, computational models have traditionally been used to estimate current flow [10][11]. Due to the human brain anatomy's diverse and unique nature, the standard practice has shifted towards employing individualized modeling approaches [12][13][14]. There are considerable doubts regarding the precision of personalized current density simulations due to the imprecision of tissue segmentation, variations in electrical conductivity within tissue types and among individuals, and the need for more reliability in electrode placement. Utilizing machine learning could encompass individual modeling and promise to enhance the accuracy and precision of tDCS current prediction. By developing a predictive model, we aim to enhance the precision and accuracy of tDCS current estimation, leading to more effective stimulation outcomes.

# **Chapter 2**

## **Related Work**

The field of electric current density mapping using MRI has been an active area of research since the late 1980s [15]. However, progress has been limited due to the relatively small research community dedicated to this field. The emergence of concurrent tDCS/MRI studies is a recent development made possible by the availability of MRI-compatible tDCS systems [16][17][18]. When an electrical current passes through the brain, it generates a magnetic field around the current pathway. MRI techniques can measure and map this magnetic field. To perform MRI field mapping, specialized imaging sequences are used that are sensitive to the magnetic field changes induced by the electrical currents. These sequences are designed to capture the phase information of the MRI signal, which is exposed to magnetic field variations. Our datasets are acquired through the utilization of concurrent tDCS and field mapping MRI.

A phantom experiment using MRI to detect the magnetic field induced by tDCS currents is conducted in this study [16]. The method relies on Biot-Savart law and exploits the linear relationship between direct electrical current and induced magnetic field. Understanding the changes in the magnetic field is crucial as it enables the detection of current distribution. In order to reconstruct the current density distribution, the magnetic field in all three coordinates must be known [19]. We employ these techniques to acquire the ground true value for the cylinder phantom utilizing the Biot-Savart law and extracting the current density distribution from the magnetic field of three coordinates using Maxwell's equations for the sphere phantom and humans.

The human experiment studies present *in vivo* images of field distributions within the brains of subjects undergoing electrical stimulation [20][21][22]. These experiments demonstrated the capability of the proposed technique to detect a tDCS-induced magnetic field as small as a nanotesla with millimeter spatial resolution. One study introduces a new imaging technique that allows for the simultaneous mapping of markers of tDCS currents and the brain's response to tDCS [22]. We utilized their result as a baseline comparison against computer simulations, where the highest correlation between MRI measurement and computer simulation is 0.79 and 0.45 on average for seven human subjects.

Several open-source computer simulations are available, including ROAST [13] and SimNIBS [23]. ROAST (Realistic Volumetric-Approach to Simulate Transcranial Electric Stimulation) aims to provide a comprehensive pipeline for simulating transcranial electrical stimulation (TES) using realistic volumetric anatomy. We utilize this tool to generate computer simulation results compared to our machine learning approach.

There have been limited publications on machine learning to detect tDCS-induced currents [9]. Typically machine learning classification methods are commonly applied in tDCS studies. For instance, one study achieved 86% accuracy in identifying working memory improvement in tDCS treatment using a Support Vector Machine (SVM) [24]. In contrast, another study reached the highest accuracy of 92% by employing K Nearest Neighbor (KNN) to detect the engagement of the targeted Arcuate Fasciculus Network (AFN) [25]. To estimate the electric field during transcranial stimulation, three studies have introduced deep learning-based methods, specifically U-net, to create personalized

human head models [7][8][9], and their approaches have the potential to replace physics-based computer simulators. Although these approaches can provide real-time performance during stimulation induction, their error rates could still be higher than many physics-based simulators [9]. Another study introduces a novel approach that leverages the nonlinear relationship between Maxwell's equations, measured magnetic field, and conductivity distribution. They designed a Moving Local Windows Multi-Layer Perceptron (MLW-MLP) to visualize high-frequency conductivity distribution at Larmor frequency in the brain directly derived from the measured magnetic flux density [26]. Our proposed approach follows similar steps, including frequency calculation and Maxwell's equations to obtain electric current density, and utilizes the Multi-Layer Perceptron Neural Network model.

## Chapter 3

### Approach

#### 3.1 Subjects

##### 3.1.1 Explanation of Setup

We utilize the cylinder and the spherical phantoms, which consist of inanimate objects without specific characteristics. The cylinder phantom serves the purpose of establishing theoretical values as a reliable reference point. It features a wire connected to

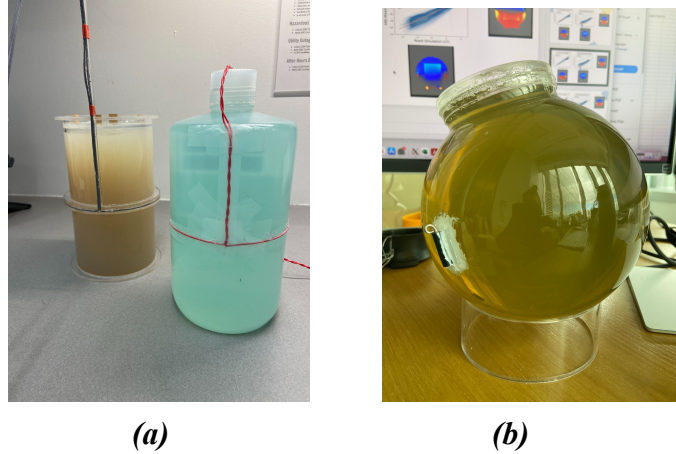


**Figure 1:** Phantom setup **(a)** Cylinder phantom **(b)** Sphere phantom

the tDCS, as shown in Figure 1 (a), generating a magnetic field that runs through the center of the cylinder without interference. This setup allows us to calculate the magnetic field accurately based on the Biot-Savart law and obtain ground truth values. The shape of a phantom can vary as long as a looped wire is wrapped around it to get the ground truth.

On the other hand, the spherical phantom is equipped with electrodes attached to its left and right sides, as shown in Figure 1 (b), resembling a setup closer to the human brain scenario. However, due to a wire connected to the electrodes, there is an interference with the tDCS-induced current, making it challenging to calculate the magnetic field on this phantom. The same limitations apply when considering the human brain case. Therefore, the spherical phantom is primarily used for prediction purposes, aiming to evaluate the optimal performance of the machine learning model trained with the cylinder dataset in an electrode setup.

In the case of human subjects, MRI images are captured during a resting state to obtain the necessary data. The positive electrode is attached to the right cortex, and the negative electrode over the left cortex.

### **3.1.2 Dataset**

The data used in this study consists of MRI 3D images with dimensions of 44 x 64 x 64. Each experiment comprises multiple sessions, and within each session, tDCS is induced twice, alternating with off states, resulting in a total of five runs, e.g., 1) sham, 2) 2mA current, 3) sham, 4) -2mA current, 5) sham. When conducting a second tDCS induction, we reverse the direction of the electric current. There are six experiments with 20 sessions for the cylinder data, seven with 23 sessions for the sphere data, and nine with 20 sessions for the human data.

To train the machine learning model, we employed the mean values from each run as features and used the theoretical values of the cylinder phantom as the target. We extracted regions of interest (ROI) from the dataset to improve the model's accuracy. The ROI for the cylinder data is 19 x 19 x 44 in 4 mm space, resulting in 15,884 records for one image, each representing the pixel value at a specific position. The ROI for the sphere data is 77 x 77 x 77 in 1 mm space; for the human brain data, it is 120 x 170 x 50.

For the development of the machine learning model, we used 18 sessions for training, resulting in 571,824 records, one session reserved for validation, yielding 31,768 records, and another session set aside for testing with the same number of records for the validation from the cylinder dataset.

## **3.2 Method**

### **3.2.1 MRI measurement and field calculations**

The cylinder phantom validates the basic frequency calculation described in formula (1), which involves determining the frequency by dividing the phase change by the corresponding time change.

$$\omega = \Delta \text{phase} / \Delta t \quad (1)$$

The magnetic field along the z-axis can also be derived using the Larmor Formula in (2).

$$\omega = \gamma B_z \quad (2)$$

By subtracting the magnetic field in the off-state from the on-state, we can obtain the tDCS-induced magnetic field, which serves as the ground truth for our machine learning training. We employ Maxwell's equation, formula (3), to calculate the direct current based on the magnetic field along three coordinates obtained through the subject rotation for the spherical phantom and human brain.

$$J = \nabla \times \beta / \mu_0 \quad (3)$$

Furthermore, the Biot-Savart law is utilized to compute the resultant magnetic field at a specific position ( $\mathbf{r}$ ) in 3D space generated by a current.

$$\mathbf{B}(\mathbf{r}) = \frac{\mu_0}{4\pi} \int_C \frac{I d\ell \times \mathbf{r}'}{|\mathbf{r}'|^3} \quad (4)$$

### 3.2.2 Machine Learning Models

This project incorporates various regression models from traditional and Deep Learning techniques. Traditional models such as Linear Regression, Bayesian Ridge Regression, Decision Tree Regression, and Stochastic Gradient Descent (SGD) Regression are employed to prioritize prediction tasks. In addition, Deep Learning models such as Multilayer Perceptron (MLP) and Convolutional Neural Network (CNN)

are utilized. The optimal model is determined through cross-validation and hyperparameter tuning to enhance performance.

### 3.3 Design

The project's initial phase involves the development of an optimal machine learning model. This process begins with an exploratory data analysis (EDA) on the dataset obtained from the cylinder phantom. Various machine learning models are then trained, fine-tuned, and validated using this dataset. The results are visualized and compared against theoretical values to determine the best-performing machine learning model.

In the second phase, the focus shifts to generating predicted magnetic field values from the optimal machine learning model on the spherical phantom and human brains. The magnetic field is also obtained from the computer simulation, ROAST, result. A comparative analysis is conducted between the predicted magnetic field values and the computer simulation result obtained from ROAST. Additionally, the predicted values are compared with MRI measurement to assess the accuracy of the outcomes.

# Chapter 4

## Machine Learning Development with Cylinder Dataset

### 4.1 Machine Learning Model Selection

Figure 2 below displays the R-squared values of each machine learning model, which serves as an essential performance metric for assessing the goodness of fit of a regression model by indicating how closely the predicted values match the actual values. Based on the results, it can be observed that the Neural Network model outperforms the conventional machine learning algorithms. Specifically, the Multilayer Perceptron (MLP) model, constructed with simple dense layers, achieves the highest score. The parameters for the conventional machine learning algorithms are set to their default values. The MLP model consists of four dense layers with ten units, while the Convolutional Neural Network (CNN) model utilizes a 1D convolutional layer. Both models employ the Adam optimizer and are trained for 100 epochs.

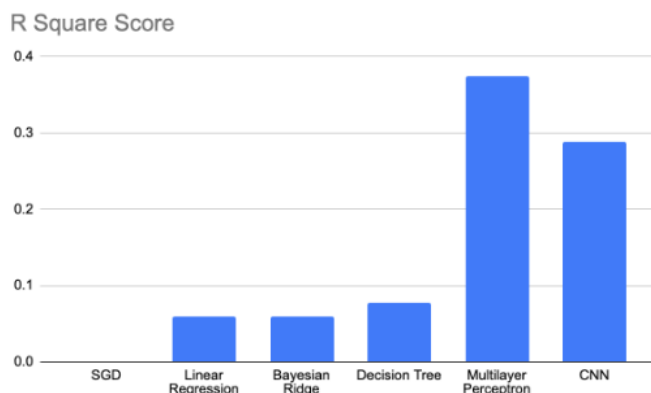


**Figure 2:** R squared of predicted value against target value on each machine learning model

## 4.2 Optimization

### 4.2.1 Layer and Unit

Figure 3 depicts a heatmap representing the optimization results of varying the number of layers and units in the Multilayer Perceptron (MLP) model. The unit size remains consistent across all layers. In each scenario, the performance of the MLP model is evaluated based on correlation, standard error, and mean squared error. The analysis aims to identify the optimal configuration. Notably, the highest score is obtained when the MLP model consists of four dense layers and three units. This configuration includes an input layer with three units, two hidden layers with three units each, and an output layer with one unit. ReLu activation is applied to the first three layers, while the output layer uses linear activation.

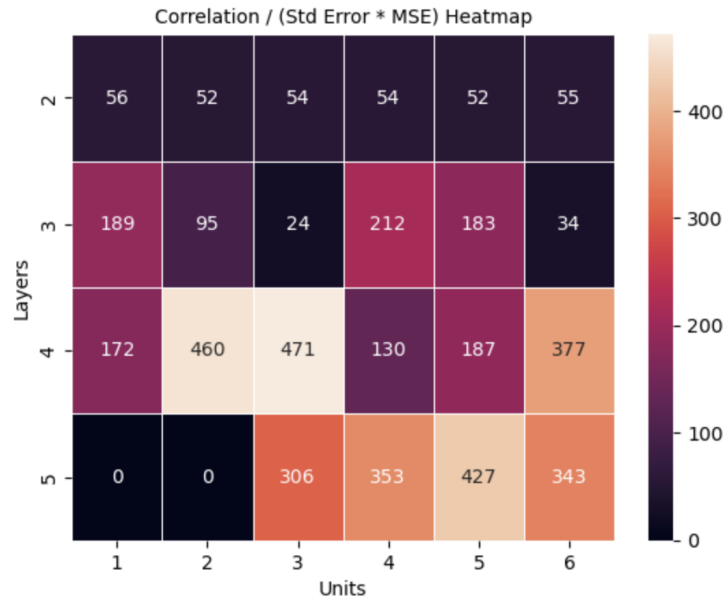


**Figure 3:** Heatmap of layer vs. unit based on Correlation, Standard Error, and Mean Squared Error on MLP

#### 4.2.2 Grid Search

Hyperparameter tuning using GridSearch was conducted to optimize the performance of the MLP model. The hyperparameters considered for optimization included the optimizer, epoch, and batch size. Specifically, the MLP model with three units in four dense layers was utilized for this process. Table 1 presents the various parameter combinations evaluated during GridSearch. Notably, among all the combinations, 18 yielded a score of over 96% in performance.

Batch size	8	16	32	64	128	256
Epoch	25	50	100	200	300	
Optimizer	Adam	Adamax	Adadelta	SGD	RMSprop	

**Table 1:** Hyperparameters for Grid Search

Furthermore, a linear regression analysis was conducted to determine the correlation between the target values and predicted values obtained from these 18 combinations. The parameter combination with the highest correlation consisted of a batch size of 64, 300 epochs, and the Adam optimizer, resulting in an impressive correlation coefficient 0.99.

### 4.3 Evaluation

Figure 4 illustrates the validation of the optimal machine learning model using the best parameters obtained in previous sections. Graph (a) reveals that the mean squared error (MSE) experiences a notable decline during the initial epochs. Subsequently, the validation MSE consistently remains lower than the training MSE shown in Graph (b)

until around 200 epochs, where it decreases again at approximately 240 epochs. Because the MLP model's performance was favorable in the previous section, we kept utilizing 300 epochs as our best performance parameter. However, in cases where execution time is a crucial factor, a reduced number of epochs between 10 and 200 could be employed.

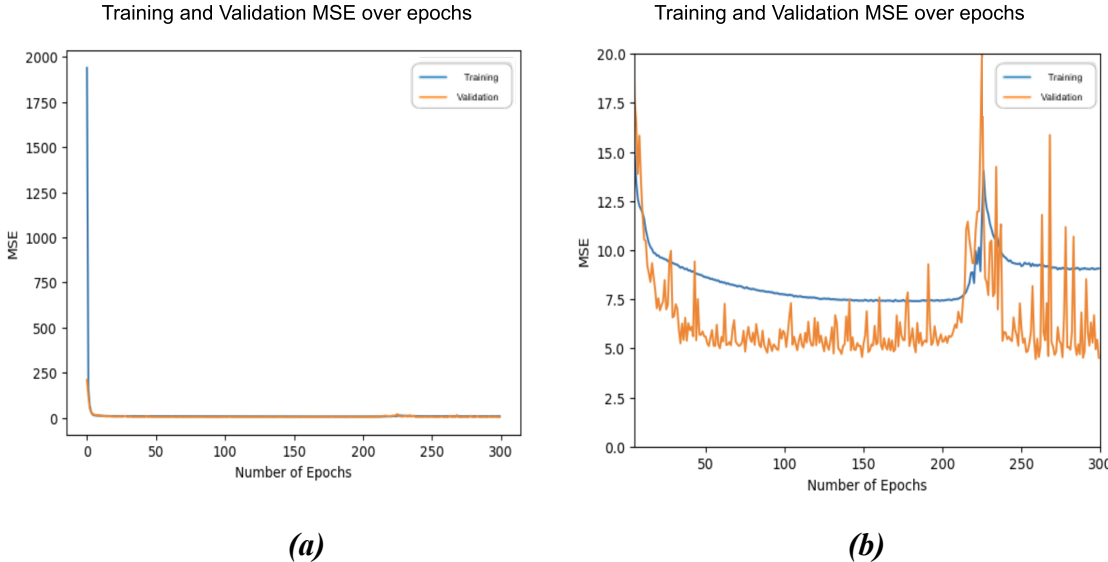


**Figure 4:** MLP model evaluation: (a) Training and Validation of MSE over the number of epochs; (b) A smaller range in the y-axis on the same plot

## 4.4 Quantitative Result for Machine Learning Testing

### 4.4.1 Cylinder ROI Images Comparison

Figures 5 and 6 exhibit the Neuroimaging Informatics Technology Initiative (NIFTI) images that depict the cylinder phantom's ROI for machine learning predictions, MRI measurement, and ground truth based on testing data. These NIFTI images are measured in nanotesla. A prediction NIFTI image is generated based on the predicted values obtained from our optimized machine learning model.

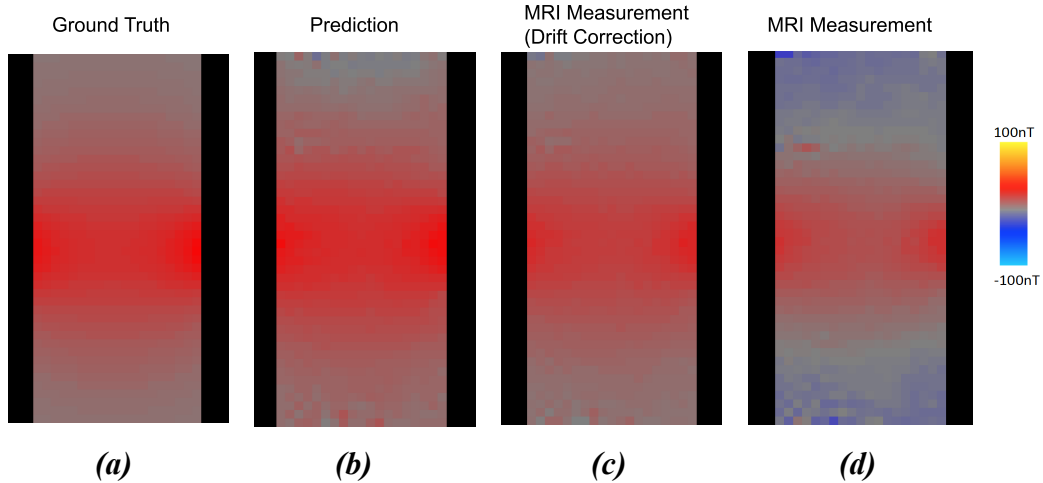


**Figure 5:** The magnetic field images of the cylinder phantom ROI along  $B_x$ : **(a)** Ground Truth **(b)** Machine Learning Prediction **(c)** MRI Measurement (drift correction) **(d)** MRI Measurement

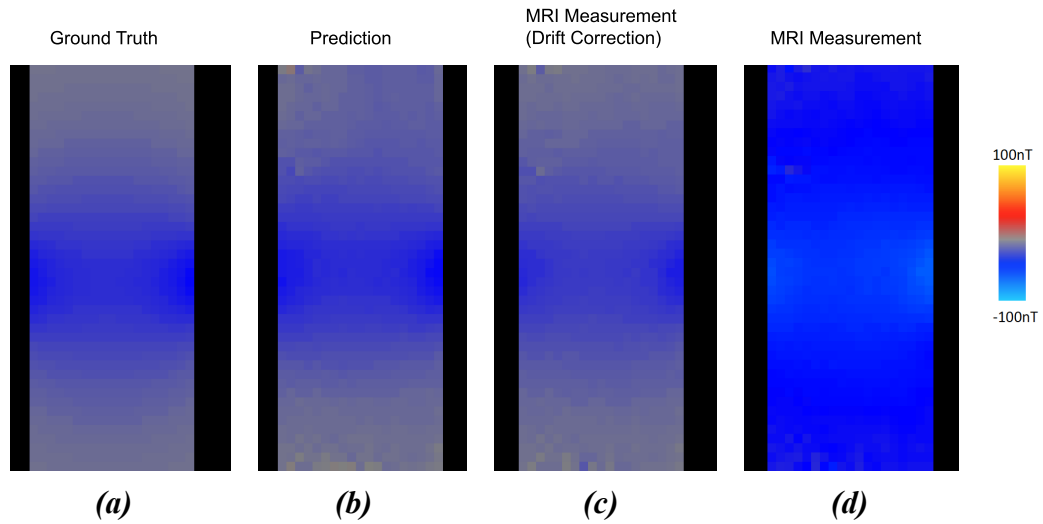


**Figure 6:** The magnetic field images of the cylinder phantom ROI along  $B_x$  in reversed polarity: **(a)** Ground Truth **(b)** Machine Learning Prediction **(c)** MRI Measurement (drift correction) **(d)** MRI Measurement

In both figures, (d) images represent the actual MRI measurement, which shows a more substantial negative value due to the shift drift during the MRI process.

Drift-corrected images are also presented in (c) for a fair comparison. It is intriguing to note that the prediction image (b) does not display any areas of drift, despite the fact that the input data originates from non-corrected drift MRI data.

Upon comparison with the ground truth images in (a), both the prediction images (b) and drift-corrected MRI measurement images (c) exhibit striking similarities. However, there is a noticeable rough transition in the gradient around the lighter color areas in both the prediction images (b) and drift-corrected MRI measurement images (c). In contrast, the ground truth images (a) demonstrate smoother transitions in the same region. Additionally, the drift-corrected MRI measurement image (c) in Figure 6 displays a slightly lighter blue around the center than the prediction and ground truth images.

#### 4.4.2 Correlation plots of Cylinder ROI

The correlation plots presented in Figure 7 illustrate the relationship between the machine learning model predictions and the ground truth values in (a), demonstrating a higher correlation than the correlation between MRI measurement and the ground truth in (b). This observation remains consistent even when considering reversed polarity of the electric current. The correlation between MRI measurement and the ground truth in (d) exhibits a significantly lower value of 0.70. Conversely, the machine learning predictions maintain a correlation of over 0.96, even in reversed polarity, as depicted in (c). These results indicate that our machine learning model can estimate the magnetic field with higher accuracy, closely aligning with the ground truth values. Based on the successful testing of our optimal MLP model in this section, we can proceed confidently to the prediction phase involving different types of datasets.

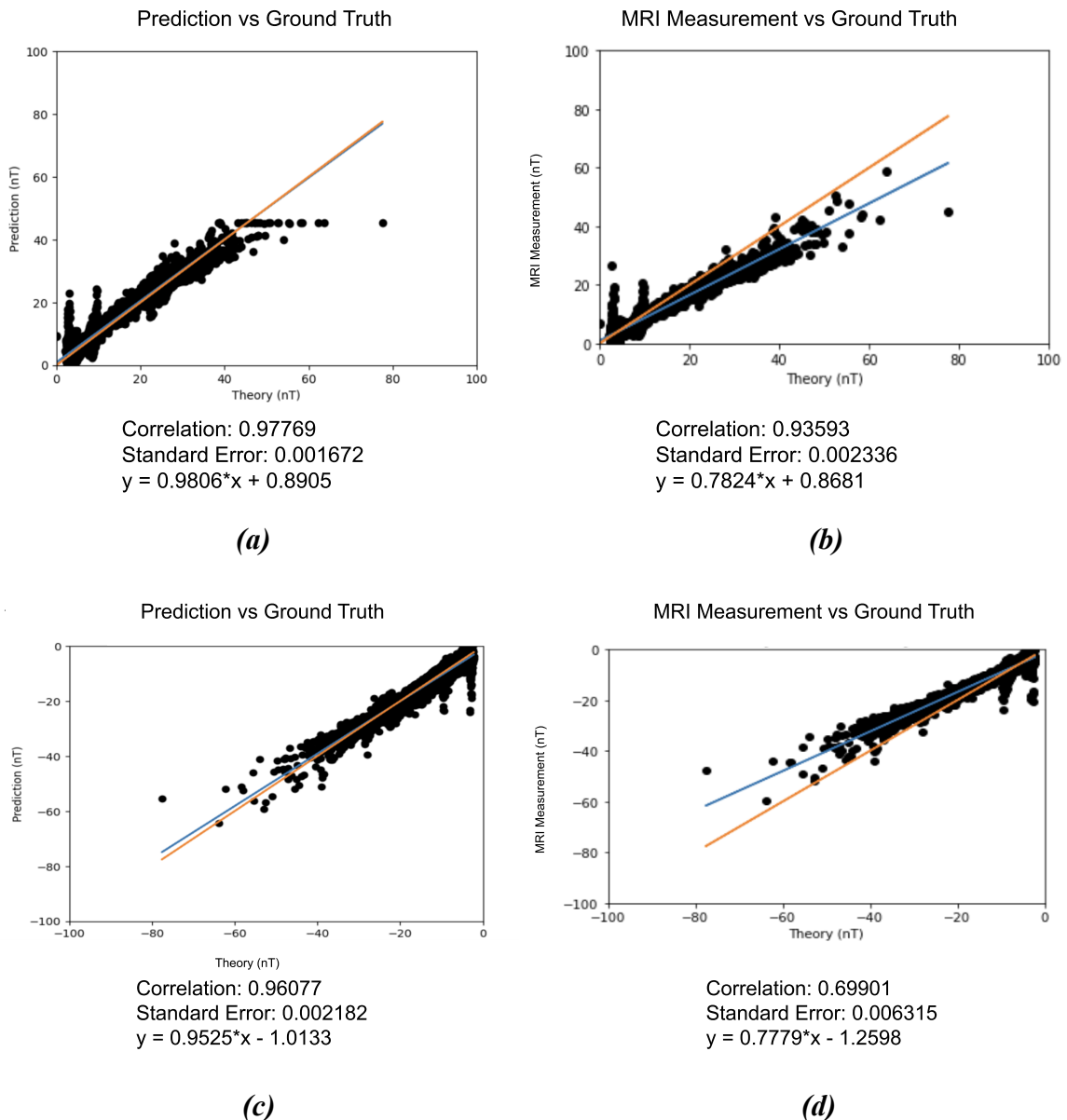


**Figure 7:** Correlation plots on the cylinder phantom ROI: (a) Prediction vs. Ground Truth (2mA) (b) MRI Measurement vs. Ground Truth (2mA) (c) Prediction vs. Ground Truth (-2mA) (d) MRI Measurement vs. Ground Truth (-2mA)

# **Chapter 5**

## **Machine Learning Evaluation on Spherical Phantom**

### **5.1 Sphere ROI Images Comparison**

In this section, we utilized our optimal MLP model obtained from the previous chapter to predict the magnetic field of the spherical dataset. Figures 8 and 9 showcase one session of images obtained from this prediction process. The square box depicted within the spherical phantom represents the ROI. We successfully obtained positive and negative magnetic field values on the spherical phantom in one image through our training machine learning process, which involved separate records for 2mA and -2mA tDCS electrical current. These values are indicative of the electric current flow occurring between them. The magnetic field derived from the ROAST result is presented as a computer simulation in (a) images. The predictions generated by our machine learning model (b) and the drift-corrected MRI measurements (c) exhibit a striking resemblance in both figures.

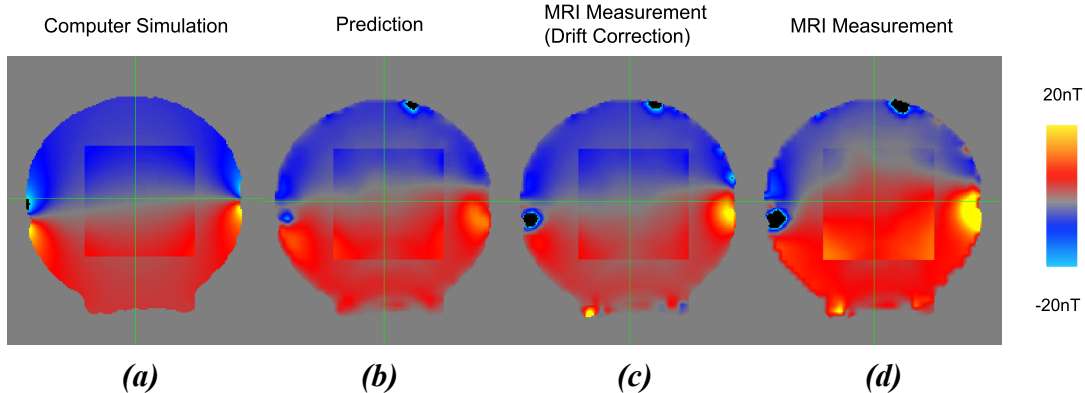


**Figure 8:** The magnetic field images of the spherical phantom along  $B_z$ : (a) Computer Simulation (b) Machine Learning Prediction (c) MRI Measurement (drift correction) (d) MRI Measurement

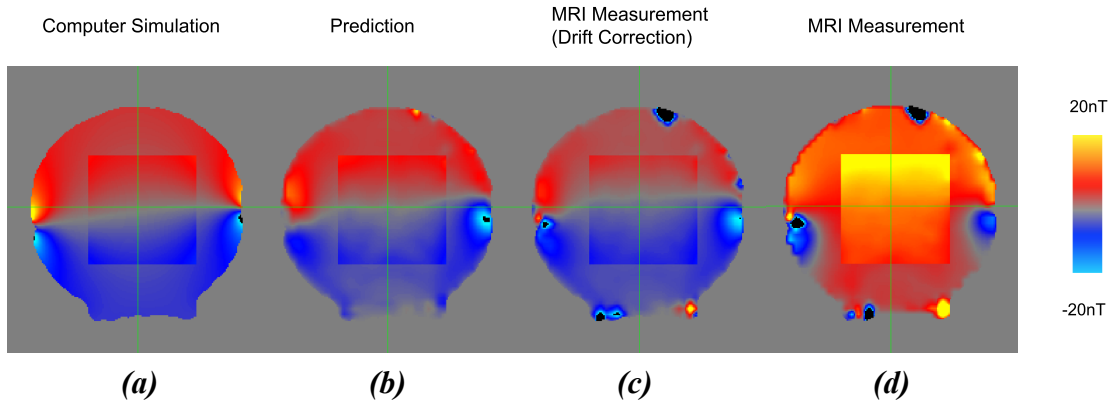


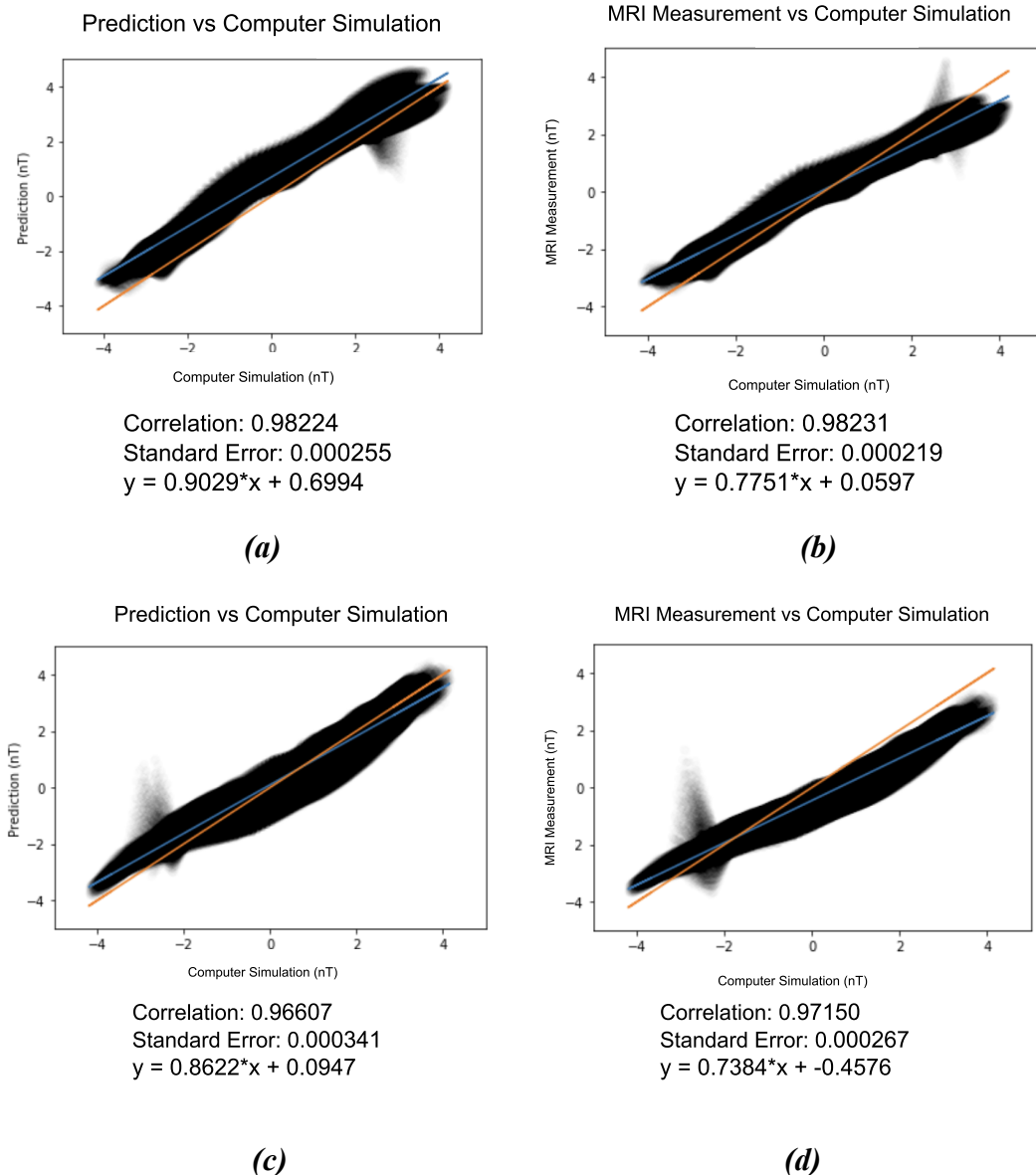
**Figure 9:** The magnetic field images of the spherical phantom along  $B_z$  in reversed polarity: (a) Computer Simulation (b) Machine Learning Prediction (c) MRI Measurement (drift correction) (d) MRI Measurement

## 5.2 Analysis of Spherical Data Prediction

### 5.2.1 Correlation of Sphere ROI

Figure 10 provides evidence of a strong correlation between prediction and computer simulation, with a value of 0.98, nearly identical to the correlation between MRI measurement and computer simulation. It is noteworthy that the majority of spherical experiments consistently demonstrate a high and comparable correlation

between prediction and MRI measurement, as indicated in Table 2 when compared to computer simulation. When comparing prediction and MRI measurement in images (e) and (f), a correlation of over 0.99 suggests that they are nearly indistinguishable or extremely similar.



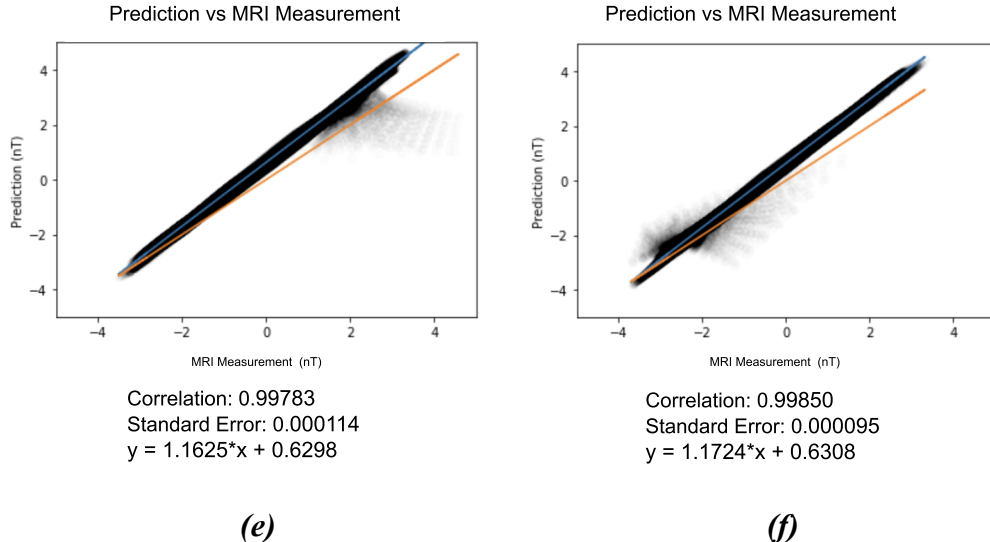


**Figure 10:** Correlation plots on the sphere phantom ROI: (a) Prediction vs. Computer Simulation (2mA) (b) MRI Measurement vs. Computer Simulation (2mA) (c) Prediction vs. Computer Simulation (-2mA) (d) MRI Measurement vs. Computer Simulation (-2mA) (e) Prediction vs. MRI Measurement (2mA) (f) Prediction vs. MRI Measurement (-2mA)

Table 2 compares nine sections of spherical data, where the correlation for 2mA tDCS induction is slightly higher compared to -2mA. The average correlation between MRI measurement and computer simulation, 0.97, with a standard deviation of 0.020, is nearly equivalent to the average correlation between prediction and computer simulation, 0.96, with a standard deviation of 0.026. Notably, the correlation between prediction and MRI measurement is consistently around 0.99, except for one session, making a standard deviation of 0.014.

		Prediction vs. CS		MRI vs. CS		Prediction vs. MRI	
		2mA	-2mA	2mA	-2mA	2mA	-2mA
<b>Sphere 1</b>	<b>Section 1</b>	0.974	0.965	0.976	0.978	0.998	0.996
	<b>Section 2</b>	0.982	0.966	0.982	0.972	0.998	0.999
	<b>Section 3</b>	0.935	0.980	0.949	0.977	0.998	0.998
<b>Sphere 2</b>	<b>Section 1</b>	0.979	0.936	0.984	0.952	0.994	0.998
	<b>Section 2</b>	0.962	0.961	0.955	0.955	0.997	0.998
<b>Sphere 3</b>	<b>Section 1</b>	0.925	0.896	0.943	0.908	0.995	0.995
	<b>Section 2</b>	0.977	0.925	0.982	0.975	0.996	0.940
	<b>Section 3</b>	0.981	0.972	0.983	0.974	0.998	0.999
<b>Each Mean</b>		0.964	0.950	0.969	0.961	0.997	0.990
<b>Each SD</b>		0.022	0.029	0.017	0.024	0.002	0.020
<b>Overall Mean</b>		0.957		0.965		0.994	
<b>Overall SD</b>		0.026		0.020		0.014	

*Table 2: Correlations comparison of the sphere ROI for three experiments*

### 5.2.2 Correlations of Whole Sphere

Interestingly, a significant contrast is observed when comparing the entire spherical phantom image, as indicated by the notable differences in correlation results in Table 3. The correlations obtained for the whole sphere exhibit considerably lower values than those observed within the ROI, despite the prediction image still achieving correlations above 0.79 against the computer simulation image. This implies that prediction surpasses MRI measurement in terms of accuracy against computer simulation. Moreover, the correlation between prediction and MRI measurement and between MRI measurement and computer simulation is exceptionally low, indicating a substantial disparity in MRI measurement when considering the entire sphere.

	ROI		Whole Sphere	
	2mA	-2mA	2mA	-2mA
Prediction vs. CS	0.982	0.966	0.798	0.825
MRI vs. CS	0.982	0.972	0.178	0.123
Prediction vs. MRI	0.998	0.999	0.128	0.125

**Table 3:** Correlations comparison of the sphere ROI and the whole sphere

At the conclusion of this section, we have achieved highly accurate prediction values, particularly within the ROI, indicating the strong performance of our machine learning prediction in an ideal scenario, the spherical phantom, compared to MRI measurement. These results demonstrate the near-perfection of our prediction, highlighting its effectiveness in this particular setting.

## Chapter 6

### Prediction on Human Brain

#### 6.1 Human Brain ROI Image Comparison

Once we confirmed the effectiveness of our MLP model in phantom cases, we applied the model to human brain data to estimate the magnetic field in the human brain. This section explicitly emphasizes examining 2mA tDCS electrical current induction. MRI measurement in reversed polarity tends to introduce more drift, noise, and artifacts that pose challenges in achieving accurate and reliable comparisons.

The resulting images in Figure 11, which show three orthogonal slices that intersect the center of the brain, reveal notable differences between MRI measurement and machine learning prediction images. The MRI measurement image (c) exhibits significant noise around the brain's edges around the green circle area. In contrast, the machine learning model successfully mitigated such noise, as observed in its prediction image (b). Additionally, in MRI measurement image (c), an artifact is visible within the yellow circle area. However, this artifact is also effectively removed in the machine learning model's prediction image (b).

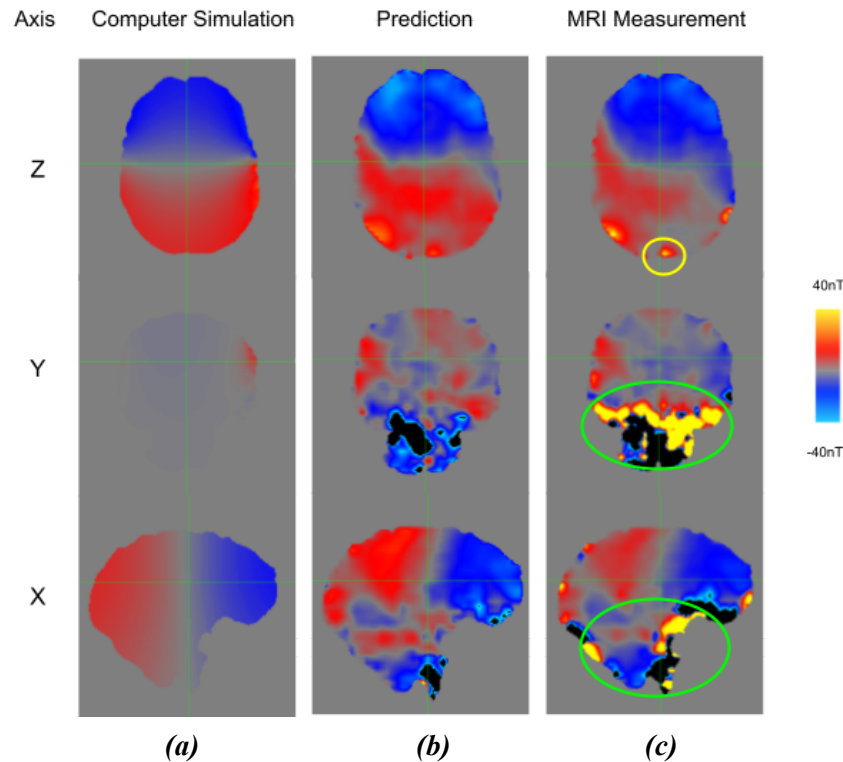


**Figure 11:** The magnetic field images of the human brain: (a) Computer Simulation (b) Machine Learning Prediction (c) MRI Measurement

Figure 12 displays the NIFTI images of both MRI-based and prediction-based, illustrating the magnetic field of the entire human head. The image (a) derived from MRI

exhibits noticeable noises in the bones and skin. Conversely, the machine learning model successfully eliminates these noises from the bone and skin regions, showcasing the advantage of utilizing machine learning for magnetic field prediction.

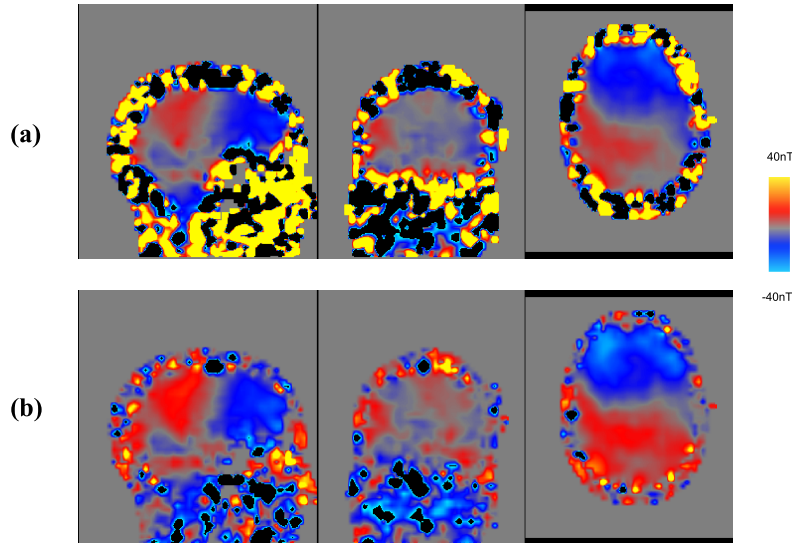


**Figure 12:** The magnetic field images of the human head (a) MRI Measurement (b) Machine Learning Prediction

## 6.2 Analysis of Human Brain Prediction

### 6.2.1 Correlation Plots of Human Brain ROI

Regarding the human brain ROI, Plot (a) demonstrates a correlation of 0.87 between prediction and computer simulation, which surpasses the correlation of 0.74 observed between MRI measurement and computer simulation, indicating that the machine learning model can accurately predict the magnetic field in closer alignments with the computer simulation result. In Figure 13 (c), the comparison between prediction-based and MRI-based images yielded a correlation of 0.85 which means our prediction image is also similar to the MRI measurement image.

Notably, our machine learning model's prediction demonstrated a higher correlation result of 0.87, compared to the correlation obtained between MRI measurement and state-of-the-art computer simulation, which achieved a maximum correlation of 0.79 in the study by Jog et al. [22]. These findings highlight the superior performance of our optimal machine learning model in terms of prediction accuracy, surpassing the capabilities of current cutting-edge techniques.

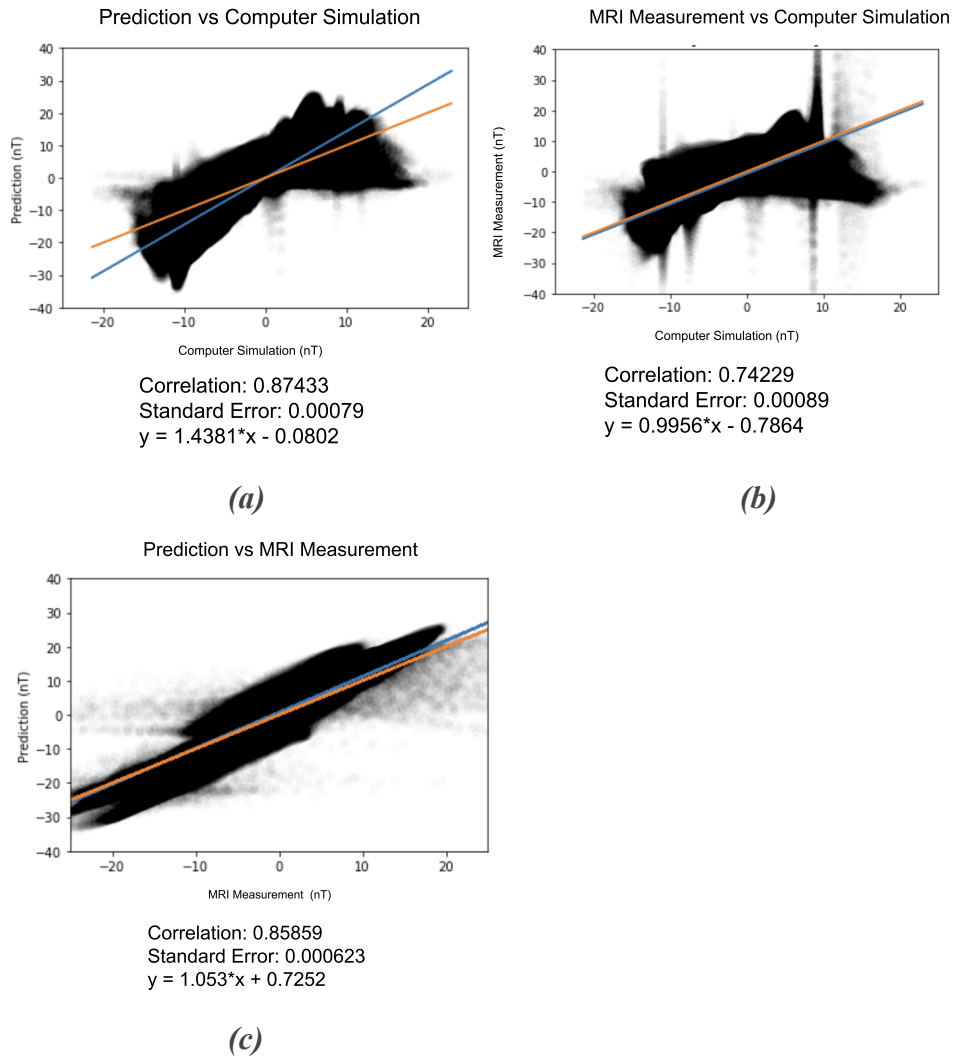


**Figure 13:** Correlation plots on the human brain ROI: (a) Prediction vs. Computer Simulation (b) MRI Measurement vs. Computer Simulation (c) Prediction vs. MRI Measurement

### 6.2.2 Correlation on Whole Brain

When examining the results for the entire brain, the correlation between prediction and computer simulation decreases by more than 50%, as shown in Table 4. However, compared to the correlation between MRI measurement vs. computer simulation, the correlation between prediction vs. computer simulation remains significantly higher.

Due to the substantial amount of noise in MRI measurement, the correlation between prediction and MRI measurement is now very low, resulting in a significant disparity between these two.

	ROI	Whole Brain
Prediction vs. CS	0.874	0.442
MRI vs. CS	0.742	0.060
Prediction vs. MRI	0.859	0.295

*Table 4: Correlation comparison of the human brain ROI and the entire brain*

### 6.3 Analysis of Three Subjects

Lastly, Figure 14 and Table 5 present the results of the magnetic field images for three individuals. The machine learning prediction exhibits higher correlations with computer simulation than MRI measurement for Subjects 1 and 2, with values of 0.87 compared to 0.74 and 0.45 compared to 0.31, respectively. However, Subject 3 shows a stronger correlation between MRI measurement and computer simulation, with values of 0.55, compared to the 0.46 of the prediction case, as indicated in Table 5. On average, the

machine learning prediction demonstrates a slightly higher correlation of 0.59 with a standard deviation of 0.242, compared to the MRI measurement of 0.54 with a standard deviation of 0.215 against computer simulation. In human brain experiments, the correlation between the prediction image and MRI measurement image remains high, such as 0.86 and 0.80 for Subjects 1 and 3, with an average of 0.74 with a standard deviation of 0.166. This indicates that the prediction image is more similar to the MRI measurement image than the ROAST computer simulation image.

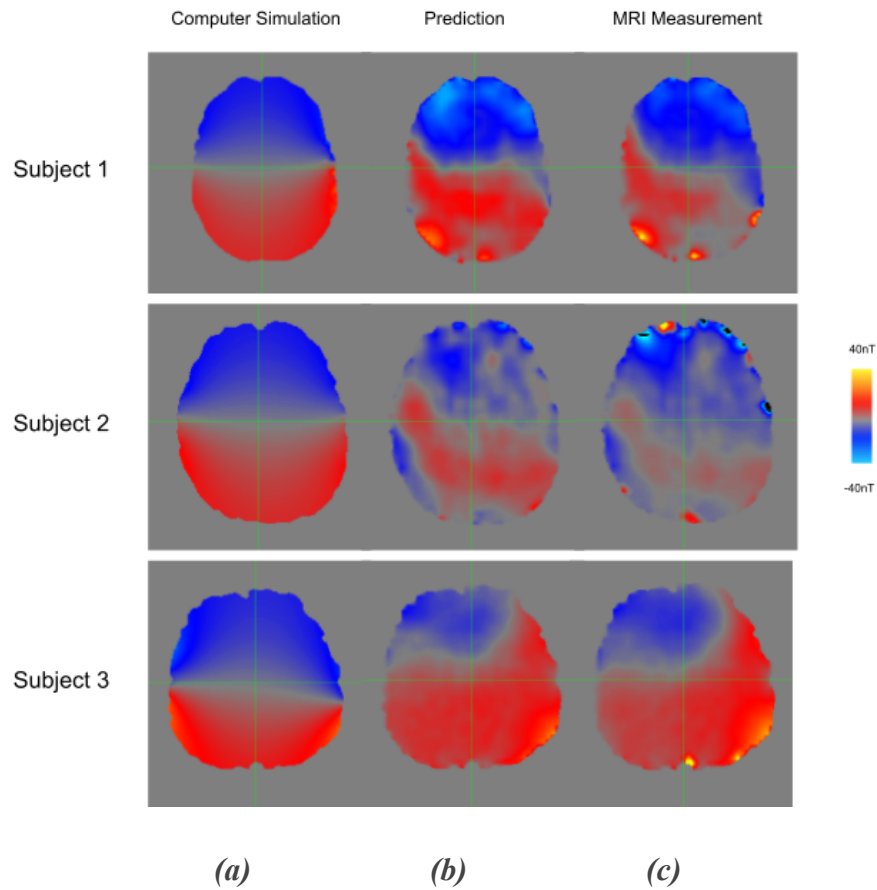


**Figure 14:** The magnetic field images of three human subjects **(a)** Computer Simulation **(b)** Machine Learning Prediction **(c)** MRI Measurement

	<b>Subject 1</b>	<b>Subject 2</b>	<b>Subject 3</b>	<b>Mean</b>	<b>SD</b>
<b>Prediction vs. CS</b>	0.874	0.450	0.459	0.594	0.242
<b>MRI vs. CS</b>	0.742	0.313	0.552	0.536	0.215
<b>Prediction vs. MRI</b>	0.859	0.550	0.808	0.739	0.166

**Table 5:** Correlation comparison of the human brain ROI of three subjects

In comparison to the state-of-the-art computer simulation results compared to their MRI measurement, which achieved a maximum correlation of 0.79 and an average correlation of 0.45 [22], our machine learning prediction achieves the highest correlation of 0.86 and an average correlation of 0.74 with our MRI measurement. This significantly surpasses the state-of-the-art results.

## Chapter 7

### Discussion and Conclusion

#### 7.1 Discussion

We acquired the ground truth values for our machine learning model from the cylinder phantom experiment by employing the Biot-Savart law on a circular looped wire. Theoretically, we could generate ground truth values for the spherical phantom using a physics-based computational model [10]. For the computer simulation result of the spherical phantom and human brain, we relied on ROAST. It is essential to mention that while ROAST allows us to specify the conductivity of various segments, such as skin

and bone, the human brain exhibits variations and inhomogeneity within each segment.

This variability significantly impacts the result, even for the spherical phantom.

Consequently, we could not utilize the ROAST result as the ground truth. However, we did not require the ground truth for the spherical phantom or the human brain, as our MLP model achieved high accuracy by sole training on cylinder phantom datasets.

## 7.2 Future Work

For future research, it is crucial to expand the testing of our MLP model to a larger sample of human subjects in order to identify the accuracy of the result and any necessary adjustments that may improve prediction performance across different individuals. Furthermore, as highlighted in the analytical section, extending prediction capabilities to encompass the entire human brain is imperative.

In addition, it is essential to acknowledge that our study did not account for scenarios involving angled wires connected to the electrodes. We specifically used parallel wiring to ensure no interference with the tDCS-induced current. However, angled wiring is more common when a human subject is inside an MRI machine, which can potentially introduce disturbance with the electric current flow. Therefore, future investigations should consider corporating this factor into the prediction model.

## 7.3 Conclusion

In conclusion, using a simple Neural Network machine learning model trained solely on a phantom wrapped in a circular wire loop, regardless of the shape of the

phantom, proved highly effective in predicting the magnetic field in the human brain. Remarkably, the machine learning model successfully mitigated noise while preserving the essential features of MRI measurement. However, it is important to note that the outcomes were influenced by the selection of the brain's region of interest (ROI). This highlights the need for further enhancements to achieve a more comprehensive machine learning model applicable to the entire brain. Nevertheless, this study provides compelling evidence that the machine learning approach offers a proof of concept for future precision of tDCS-induced electric currents prediction.

## Bibliography

- [1] Ferrucci, Roberta, F. Mameli, I. Guidi, S. Mrakic-Sposta, M. Vergari, S. E. E. A. Marceglia, F. Cogiamanian, S. Barbieri, E. Scarpini, and A. Priori. "Transcranial direct current stimulation improves recognition memory in Alzheimer disease." *Neurology* 71, no. 7 (2008): 493-498.
- [2] Nitsche, Michael A., Paulo S. Boggio, Felipe Fregni, and Alvaro Pascual-Leone. "Treatment of depression with transcranial direct current stimulation (tDCS): a review." *Experimental neurology* 219, no. 1 (2009): 14-19.
- [3] Coffman, Brian A., Vincent P. Clark, and Raja Parasuraman. "Battery powered thought: enhancement of attention, learning, and memory in healthy adults using transcranial direct current stimulation." *Neuroimage* 85 (2014): 895-908.

- [4] Zacharaki, Evangelia I., Sumei Wang, Sanjeev Chawla, Dong Soo Yoo, Ronald Wolf, Elias R. Melhem, and Christos Davatzikos. "Classification of brain tumor type and grade using MRI texture and shape in a machine learning scheme." *Magnetic Resonance in Medicine: An Official Journal of the International Society for Magnetic Resonance in Medicine* 62, no. 6 (2009): 1609-1618.
- [5] Salvatore, Christian, Antonio Cerasa, Petronilla Battista, Maria C. Gilardi, Aldo Quattrone, Isabella Castiglioni, and Alzheimer's Disease Neuroimaging Initiative. "Magnetic resonance imaging biomarkers for the early diagnosis of Alzheimer's disease: a machine learning approach." *Frontiers in neuroscience* 9 (2015): 307.
- [6] Kavakiotis, Ioannis, Olga Tsave, Athanasios Salifoglou, Nicos Maglaveras, Ioannis Vlahavas, and Ioanna Chouvarda. "Machine learning and data mining methods in diabetes research." *Computational and structural biotechnology journal* 15 (2017): 104-116.
- [7] Yokota, Tatsuya, Toyohiro Maki, Tatsuya Nagata, Takenobu Murakami, Yoshikazu Ugawa, Ilkka Laakso, Akimasa Hirata, and Hidekata Hontani. "Real-time estimation of electric fields induced by transcranial magnetic stimulation with deep neural networks." *Brain stimulation* 12, no. 6 (2019): 1500-1507.
- [8] Rasheda, Essam A., Jose Gomez-Tamesa, and Akimasa Hirataa. "Development of accurate human head models for personalized electromagnetic dosimetry using deep learning." *arXiv preprint arXiv:2002.09080* (2020).
- [9] Jia, Xiaofan, Sadeed Bin Sayed, Nahian Ibn Hasan, Luis J. Gomez, Guang-Bin Huang, and Abdulkadir C. Yucel. "DeeptDCS: Deep Learning-Based Estimation of

Currents Induced During Transcranial Direct Current Stimulation." IEEE Transactions on Biomedical Engineering (2022).

[10] Truong, Dennis Q., Mathias Hüber, Xihe Xie, Abhishek Datta, Asif Rahman, Lucas C. Parra, Jacek P. Dmochowski, and Marom Bikson. "Clinician accessible tools for GUI computational models of transcranial electrical stimulation: BONSAI and SPHERES." *Brain stimulation* 7, no. 4 (2014): 521-524.

[11] Mahdavi, Shirin, Farzad Towhidkhah, and Alzheimer's Disease Neuroimaging Initiative. "Computational human head models of tDCS: Influence of brain atrophy on current density distribution." *Brain stimulation* 11, no. 1 (2018): 104-107.

[12] Jog, Mayank V., Robert X. Smith, Kay Jann, Walter Dunn, Belen Lafon, Dennis Truong, Allan Wu, Lucas Parra, Marom Bikson, and Danny JJ Wang. "In-vivo imaging of magnetic fields induced by transcranial direct current stimulation (tDCS) in human brain using MRI." *Scientific reports* 6, no. 1 (2016): 1-10.

[13] Huang, Yu, Abhishek Datta, Marom Bikson, and Lucas C. Parra. "Realistic volumetric-approach to simulate transcranial electric stimulation—ROAST—a fully automated open-source pipeline." *Journal of neural engineering* 16, no. 5 (2019): 056006.

[14] Bikson, Marom, Asif Rahman, Abhishek Datta, Felipe Fregni, and Lotfi Merabet. "High-resolution modeling assisted design of customized and individualized transcranial direct current stimulation protocols." *Neuromodulation: Technology at the Neural Interface* 15, no. 4 (2012): 306-315.

- [15] Joy, Mike, Greig Scott, and Mark Henkelman. "In vivo detection of applied electric currents by magnetic resonance imaging." *Magnetic resonance imaging* 7, no. 1 (1989): 89-94.
- [16] Kwon, Yong Hyun, Myoung-Hwan Ko, Sang Ho Ahn, Yun-Hee Kim, Jun Chan Song, Chu-Hee Lee, Min Cheol Chang, and Sung Ho Jang. "Primary motor cortex activation by transcranial direct current stimulation in the human brain." *Neuroscience letters* 435, no. 1 (2008): 56-59.
- [17] Meinzer, Marcus, Robert Lindenberg, Daria Antonenko, Tobias Flaisch, and Agnes Flöel. "Anodal transcranial direct current stimulation temporarily reverses age-associated cognitive decline and functional brain activity changes." *Journal of Neuroscience* 33, no. 30 (2013): 12470-12478.
- [18] Holland, Rachel, Alex P. Leff, William D. Penny, John C. Rothwell, and Jenny Crinion. "Modulation of frontal effective connectivity during speech." *NeuroImage* 140 (2016): 126-133.
- [19] Göksu, Cemil, Mehdi Sadighi, H. H. Eroğlu, and M. Eyüboğlu. "Realization of magnetic resonance current density imaging at 3 Tesla." In *2014 36th Annual International Conference of the IEEE Engineering in Medicine and Biology Society*, pp. 1115-1118. IEEE, 2014.
- [20] Göksu, Cihan, Lars G. Hanson, Hartwig R. Siebner, Philipp Ehses, Klaus Scheffler, and Axel Thielscher. "Human in-vivo brain magnetic resonance current density imaging (MRCDI)." *Neuroimage* 171 (2018): 26-39.

- [21] Kasinadhuni, A. K., A. Indahlastari, M. Chauhan, Michael Schär, T. H. Mareci, and R. J. Sadleir. "Imaging of current flow in the human head during transcranial electrical therapy." *Brain stimulation* 10, no. 4 (2017): 764-772.
- [22] Jog, Mayank, Kay Jann, Lirong Yan, Yu Huang, Lucas Parra, Katherine Narr, Marom Bikson, and Danny JJ Wang. "Concurrent imaging of markers of current flow and neurophysiological changes during tDCS." *Frontiers in Neuroscience* 14 (2020): 374.
- [23] Saturnino, Guilherme B., Kristoffer H. Madsen, and Axel Thielscher. "Electric field simulations for transcranial brain stimulation using FEM: an efficient implementation and error analysis." *Journal of neural engineering* 16, no. 6 (2019): 066032.
- [24] Albizu, Alejandro, Ruogu Fang, Aprinda Indahlastari, Andrew O'Shea, Skylar E. Stolte, Kyle B. See, Emanuel M. Boutzoukas, Jessica N. Kraft, Nicole R. Nissim, and Adam J. Woods. "Machine learning and individual variability in electric field characteristics predict tDCS treatment response." *Brain stimulation* 13, no. 6 (2020): 1753-1764.
- [25] Shinde, Anant, Sovesh Mohapatra, and Gottfried Schlaug. "Identifying the engagement of a brain network during a targeted tDCS-fMRI experiment using a machine learning approach." *PLOS Computational Biology* 19, no. 4 (2023): e1011012.
- [26] Lee, Mun Bae, Geon-Ho Jahng, Hyung Joong Kim, and Oh-In Kwon. "High-frequency conductivity at Larmor-frequency in human brain using moving local window multilayer perceptron neural network." *Plos one* 16, no. 5 (2021): e0251417.

## Appendix

	Subject 1	Subject 2	Subject 3	Mean	SD
Prediction vs. CS	0.442	0.142	0.476	0.353	0.184
MRI vs. CS	0.060	0.001	0.200	0.087	0.103
Prediction vs. MRI	0.295	0.170	0.463	0.309	0.147

*Table A1: Correlation comparison of the entire brain of three subjects*